




“Three-in-one” strategy: Heat regulation and conversion enhancement of a multifunctional separator for safer lithium–sulfur batteries

Kaiping Zhu¹ | Luhe Li¹ | Pan Xue¹ | Jun Pu²  | Liyun Wu¹ | Gengde Guo¹ | Ran Wang¹ | Ye Zhang¹ | Huisheng Peng³ | Guo Hong⁴ | Qiang Zhang⁵  | Yagang Yao¹ 

¹National Laboratory of Solid State Microstructures, College of Engineering and Applied Sciences, Jiangsu Key Laboratory of Artificial Functional Materials, Collaborative Innovation Center of Advanced Microstructures, Nanjing University, Nanjing, China

²Key Laboratory of Functional Molecular Solids, Ministry of Education, College of Chemistry and Materials Science, Anhui Normal University, Wuhu, China

³State Key Laboratory of Molecular Engineering of Polymers, Department of Macromolecular Science, Laboratory of Advanced Materials, Fudan University, Shanghai, China

⁴Department of Materials Science and Engineering, College of Engineering, City University of Hong Kong, Hong Kong, China

⁵Beijing Key Laboratory of Green Chemical Reaction Engineering and Technology, Department of Chemical Engineering, Tsinghua University, Beijing, China

Correspondence

Yagang Yao, National Laboratory of Solid State Microstructures, Jiangsu Key Laboratory of Artificial Functional Materials, Collaborative Innovation Center of Advanced Microstructures, College of Engineering and Applied Sciences, Nanjing University, Nanjing 210093, China.

Email: ygyao2018@nju.edu.cn

Funding information

National Key R&D Program of China, Grant/Award Number: 2022YFE0206500

Abstract

The safety problems encountered with lithium–sulfur batteries (LSBs) hinder their development for practical applications. Herein, a highly thermally conductive separator was constructed by cross-weaving super-aligned carbon nanotubes (SA-C) on super-aligned boron nitride@carbon nanotubes (SA-BC) to create a composite film (SA-BC/SA-C). This separator was used to fabricate safe LSBs with improved electrochemical performance. The highly aligned separator structure created a uniform thermal field that could rapidly dissipate heat accumulated during continuous operation due to internal resistance, which prevented the development of extremely high temperatures. The array of boron nitride nanosheets endowed the composite separator with a large number of adsorption sites, while the highly graphitized carbon nanotube skeleton accelerated the catalytic conversion of high-valence polysulfides into low-valence polysulfides. The arrayed molecular brush design enabled the regulation of local current density and ion flux, and considerably alleviated the growth of lithium dendrites, thus promoting the smooth deposition of Li metal. Consequently, a battery constructed with the SA-BC/SA-C separator

Kaiping zhu, Luhe li and Pan xue contributed equally to this work.

This is an open access article under the terms of the Creative Commons Attribution License, which permits use, distribution and reproduction in any medium, provided the original work is properly cited.

© 2023 The Authors. *Carbon Energy* published by Wenzhou University and John Wiley & Sons Australia, Ltd.

showed a good discharge capacity of 685.2 mAh g^{-1} over 300 cycles (a capacity decay of 0.026% per cycle) at 2 C and 60°C . This “three-in-one” multifunctional separator design strategy constitutes a new path forward for overcoming the safety problems of LSBs.

KEYWORDS

conversion enhancement, heat regulation, high safety, lithium–sulfur batteries, multifunctional separator

1 | INTRODUCTION

Compared with aqueous batteries, organic alkaline-metal batteries have attracted much more attentions because of their higher theoretical capacity and wider voltage window. However, organic alkaline-metal batteries often contain inflammable electrolytes and an unstable metal anode, which gives rise to safety problems. For example, although lithium–sulfur batteries (LSBs) are common, there are safety risks associated with their use because they contain multiple flammable substances: sulfur (as the cathode) and metallic lithium (as the anode), and organic electrolytes and organic separators. A typical LSB has a high theoretical specific capacity of 1675 mAh g^{-1} and a specific energy density of 2600 Wh kg^{-1} .^{1,2} In addition, considerable progress has been made in solving other problems of LSBs, such as their polysulfide shuttle, Li dendrite growth, and sluggish redox kinetics.^{3–5} However, few studies have devised a general approach to overcome these challenges from the perspective of thermal management. This is a problem, especially as thermal management is also crucial for significantly reducing heat accumulation during the operation of LSBs and thus subsequent side reactions and the above-mentioned safety risks associated with the flammable components of LSBs.^{6,7} Accordingly, many efforts have been made to develop safer LSBs, such as by adding noncombustible materials to electrolytes^{8,9} and constructing smart separators¹⁰ to track dendrite growth and provide early warnings of flammability. However, such approaches do not eliminate the risk of battery fires, especially in LSBs containing high concentrations of Li metal.

Continuous heat accumulation¹¹ and instantaneous combustion^{12,13} are the root causes of the safety problems of LSBs. A large amount of heat can be released and side reactions can occur when LSBs are exposed to electrical, mechanical, or thermal conditions that exceed the design limits of an LSB, such as when an LSB is overused.¹⁴ When heat released within an LSB cannot be dissipated efficiently, the LSB rapidly increases in temperature,

which exacerbates problems such as electrolyte decomposition and cathode polarization. Moreover, the Li dendrites that grow irreversibly on the anode of an LSB can ultimately pierce its separator, further aggravating the risk of thermal runaway that can result in combustive or explosive failure.^{14–16}

These safety risks can be alleviated by the appropriate management of heat accumulation in the interior of LSBs, and some strategies have been devised.^{17,18} Thermal runaway can be prevented by adding external thermal protection, such as maintaining an LSB under a large airflow, building a cooling vent into an LSB case, and constructing a heat transfer system.¹⁹ Unfortunately, these external measures cannot rapidly dissipate heat generated in a high-intensity operating state.²⁰ Thus, internal measures are needed; that is, the key protective components must be located within the LSB.²¹ For example, a separator coated with aluminum nitride, which has a high thermal conductivity, was shown to provide a well-distributed thermal interface that evacuated accumulated heat, thus preventing cracks in the solid electrolyte interphase film and suppressing dendrite growth.^{22–24} In other approaches, a flexible freestanding graphene–tin oxide film electrode with high thermal conductivity enabled heat dissipation, thus alleviating LSB overheating,²⁵ while a rationally designed separator based on phase-change materials was found to restrain rapidly increasing temperatures in an LSB.²⁶

The polysulfide shuttle effect and Li dendrite growth in LSBs should also be considered to enhance LSB safety. This is because the dissolution and shuttling of polysulfides cause a rapid increase in internal resistance, resulting in further heat generation during the charging and discharging processes, and because, as mentioned, dendrites can pierce the separator of LSB, thereby causing short-circuiting.^{27–31} The latter results from the fact that the separator is in direct contact with the cathode and the anode to prevent short-circuiting while allowing ion transport.^{32–34} Separator functionalization is regarded as a simple and effective method to simultaneously regulate the dissolution/deposition behavior of

Li ions and constrain the interfacial multi-electron reaction of polysulfides in LSBs.^{35–37} It would therefore be beneficial to simultaneously solve the above-mentioned problems of LSBs by developing an appropriately modified separator.

Herein, we describe our construction of a highly thermally conductive separator, which we achieved by cross-weaving super-aligned carbon nanotubes (SA-C) onto super-aligned boron nitride@carbon nanotubes (SA-BC) to create a composite film. This unique super-aligned structure formed a homogeneous thermal field with a high theoretical thermal conductivity of $2000 \text{ W m}^{-1} \text{ K}^{-1}$.^{38,39} The double-layer super-aligned structure with a homogeneous thermal field rapidly dispersed heat generated by the LSB's internal resistance during charging and discharging, thereby preventing continuous increases in temperature. In addition, boron nitride (BN) has a strong affinity for polysulfides and therefore suppresses the polysulfide shuttle effect. Specifically, the straight ion-transport channels in the composite structure, combined with its smooth conduction of electrons, enhanced the capture of high-valence polysulfides and accelerated their catalytic conversion into low-valence sulfides. The super-aligned staggered structures wrapped by BN nanosheets also created a molecular brush effect that homogenized ion flow, thus alleviating the dendrite growth caused by high local concentrations of ions. In this way, the smooth deposition of Li metal was promoted. Furthermore, BN is noncombustible, which eliminated the risk of organic separator combustion. As a result, the LSB that we constructed using the SA-BC/SA-C separator showed considerable thermal management ability and excellent electrochemical performance. It had high rate performance (541.5 mAh g^{-1} at 5 C) and excellent cycling stability (a low capacity decay rate of 0.026% at 2 C over 300 cycles) at a high operating temperature (60°C). Moreover, even at a high sulfur loading (3 mg cm^{-2}), the LSB with an SA-BC/SA-C separator delivered a high discharge capacity (588.6 mAh g^{-1} at 0.3 C over 100 cycles). This high thermal conductivity of this super-aligned design provides a new research approach for developing safer LSBs with high energy densities.

2 | RESULTS AND DISCUSSION

Carbon nanotube (CNT) networks were grown from iron/alumina/ethylene precursors by chemical vapor deposition under an argon/hydrogen atmosphere. A typical soft-lock drawing method was then used to cross-weave horizontally aligned CNT arrays to form an SA-C film from random CNT networks. BN nanosheets

were then grown surrounding the aligned CNT bundle array templates to form an SA-BC film. Subsequently, the soft-lock drawing method was again used to assemble the SA-BC/SA-C composite separator (Figure S1). The detailed fabrication procedures are described in the Experimental Section.

As shown in Figure 1A, the SA-BC film close to the anode showed a homogeneous thermal field due to the high thermal conductivity of the BN and the CNTs, which effectively dissipated the accumulated heat generated inside the LSB, thus preventing battery being over-heated, whereas the commercial Celgard separator lacked this ability (Figure 1B). The BN nanosheet array had many adsorption sites that captured the free polysulfides in the electrolyte. Moreover, at the BN–CNT interface, the high conductivity of CNTs provided a relatively fast and smooth channel for electron transport, which accelerated the catalytic conversion of high-valence polysulfides into low-valence polysulfides, and evacuated the heat accumulated due to the high internal resistance in the electrolyte caused by polysulfide dissolution (Figure 1C). These features constitute an improvement over the Celgard separator (Figure 1D). In addition, the straight ion-transport channels combined with the molecular brush effect homogenized the ion concentration, enabling the smooth deposition of Li metal and thereby preventing separator piercing that could cause short-circuiting. In contrast, the zigzag ion channels of the Celgard separator cause an uneven distribution of ion concentration, leading to substantial growth of Li dendrites. Thus, LSBs with SA-BC/SA-C separators suppressed polysulfide shuttling and dendrite growth, and are thus much safer than other types of LSBs.

The results of the detailed structure and morphology characterization of the SA-BC/SA-C separator are shown in Figure 2. The scanning electron microscopy (SEM) images show a free-woven form in which the SA-C is cross-woven over the SA-BC film. In this way, the thickness and porosity of the separator are controlled according to the required LSB performance (Figure 2A). This super-aligned structure tended to form a homogeneous thermal field with smooth ion-transfer channels, which facilitated the dissipation of accumulated heat. The SA-BC was derived from smooth SA-C (Figure 2D) on which dense BN nanosheets grew around CNT nanobundles (Figure 2B,C). The dense BN nanosheets acted as anchoring sites that constrained the shuttling behavior of polysulfides. Meanwhile, the BN nanosheet structure created a molecular brush effect that homogenized the ion flow and thus hindered dendrite growth. In contrast, the commercial Celgard separator showed an uneven distribution of pores with zigzag ion-transfer channels, which did not inhibit polysulfide shuttling or the growth of dendrites (Figure S2).

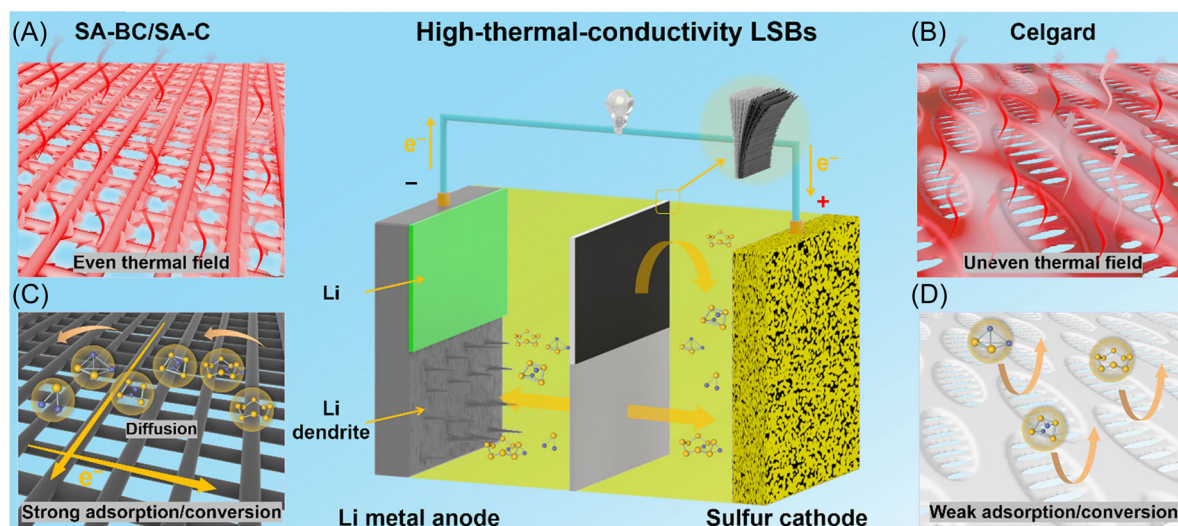


FIGURE 1 Schematic illustration of the SA-BC/SA-C separator applied in a lithium-sulfur battery. (A) SA-BC structure with a homogeneous thermal field. (B) Celgard separator without a uniform thermal field. The SA-BC/SA-C separator effectively suppressed polysulfide shuttling and lithium dendrite growth, while the Celgard separator did not. (C) SA-C structure with a smooth electron-transfer pathway that accelerated polysulfide adsorption and conversion. (D) Celgard separator that did not accelerate polysulfide adsorption and conversion.

Transmission electron microscopy (TEM) images further confirmed the composite structure of the BN nanosheets surrounding the CNT nanobundles (Figure 2E). High-resolution TEM and selected-area electron diffraction were also utilized to prove that the nanosheets were composed of few-layer-thick hexagonal BN nanosheets (Figure S3). Furthermore, scanning TEM and energy-dispersive spectroscopy mapping of the SA-BC nanobundles demonstrated that there was an even distribution of carbon, boron, and nitrogen on the CNT surface (Figure 2F). X-ray diffraction (XRD) analysis was conducted to confirm the crystal structure of SA-BC. As shown in Figure 2G, the XRD patterns of SA-BC showed two main diffraction peaks, (002) and (100), which are attributed to BN (PDF#73–2095), and a broad diffraction peak (002) of CNTs (PDF#75–2078).^{40,41} The Raman spectrum showed two distinct peaks at 1350 and 1580 cm^{-1} , which are the D and G peaks of the CNTs, respectively. It also contained a peak at 1370 cm^{-1} corresponding to the E_{2g} vibration mode of hexagonal-BN, suggesting that the dense BN nanosheets completely wrapped the CNT nanobundles (Figure 2H).^{42,43} X-ray photoelectron spectroscopy (XPS) analysis was used to determine the surface composition and morphology of SA-BC (Figures 2I and S4). The peaks at 190.6 and 398.1 eV, respectively, in the high-resolution B 1s and N 1s spectra correspond to B–N bond, indicating the successful preparation of BN.^{44,45}

Other tests were conducted to further demonstrate the suitability of SA-BC/SA-C as a safe separator for use in

LSBs. As shown in Figure 3A, the SA-BC/SA-C separator had an appropriate thickness of 580 μm , which could be adjusted by changing the number of woven layers. The white side of the separator, corresponding to SA-BC, was close to the Li anode, while the black side, corresponding to SA-C, was close to the sulfur cathode. BN tends to accumulate polysulfides owing to its poor electrical conductivity, which decreases further adsorption and anchoring process, thus failing to fundamentally solve the shuttling problem of polysulfides. Therefore, we combined BN with highly conductive CNTs to realize the rapid charge transfer of polysulfides in the redox process. This promoted the conversion of high-valence polysulfides into low-valence polysulfides, thereby preventing the accumulation of polysulfides and the subsequent loss of adsorption sites. In addition, the high mechanical strength of BN physically inhibited dendrite growth. Specifically, the molecular brush effect of the BN nanosheet array significantly homogenized the ion flow, preventing the uneven spatial distribution of ions and thus dendrite growth, which increased the safety of the LSB.^{46,47} The SA-BC/SA-C separator showed good foldability and flexibility, suggesting that it has potential applications in flexible energy-storage devices. Electrolyte contact-angle measurements were performed to investigate the wettability of the electrolyte. As shown in Figure 3B, the SA-BC/SA-C separator had a contact angle of 18.24°, which was smaller than that of the Celgard separator (29.97°). Moreover, the contact-angle measurements of various separators by using an electrolyte with tiny polysulfides were carried out to

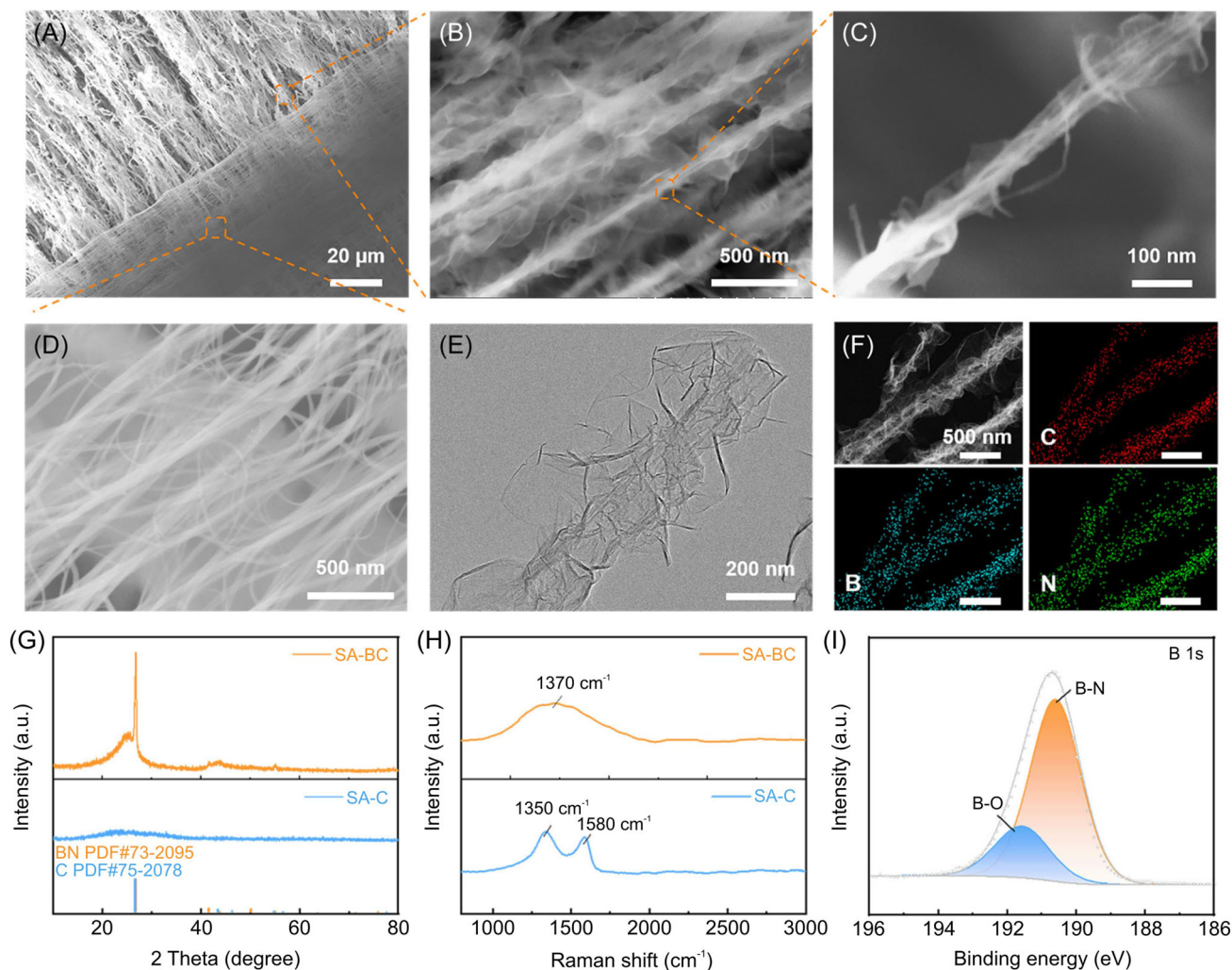


FIGURE 2 Structure and morphology characterization of the SA-BC/SA-C separator. (A) Scanning electron microscopy images of an SA-BC/SA-C, (B, C) SA-BC, and (D) SA-C. (E) Transmission electron microscopy and (F) elemental mapping images of SA-BC. (G) X-ray diffraction patterns, (H) Raman spectra, and (I) high-resolution X-ray photoelectron spectra of B 1s for SA-BC and SA-C.

simulate the wettability under actual conditions (Figure S5). Similarly, the SA-BC/SA-C separator also showed a smaller contact angle due to the uniform and dense pore structure, which will be more conducive to the infiltration of the electrolyte. These results indicate that the SA-BC/SA-C separator accelerated electrolyte infiltration, thus promoting Li-ion transfer and enhancing electrochemical performance.

As a separator with high temperature tolerance enhances LSB safety performance, we examined whether our separator had this property. As shown in Figure 3C, the SA-BC/SA-C separator maintained a constant shape as the temperature was increased from 30°C to 60°C, while the Celgard separator failed to withstand this temperature change, and became wrinkled and melted. This high temperature tolerance of the SA-BC/SA-C separator reduces the safety risk caused by separator contraction due to heat accumulation, and would allow

an LSB to operate under extreme conditions. Combustion experiments were also carried out to further demonstrate the potential application of the composite separator in extreme environments. As shown in Figure S6, the separator did not ignite when placed in a flame and remained intact after removal from the flame. In contrast, the Celgard separator quickly ignited. To further clarify the superior heat management of the SA-BC/SA-C separator, heat dissipation measurements were conducted. An infrared thermal imager was used to monitor the temperature change of the surface of a light-emitting diode (LED) that had the separator attached under its radiator. As shown in Figures 3D and S7, the surface temperature of the LED equipped with the SA-BC/SA-C separator was lower than that of the LED equipped with the Celgard separator over the same operation time. This result indicates that the SA-BC/SA-C separator created a uniform thermal field

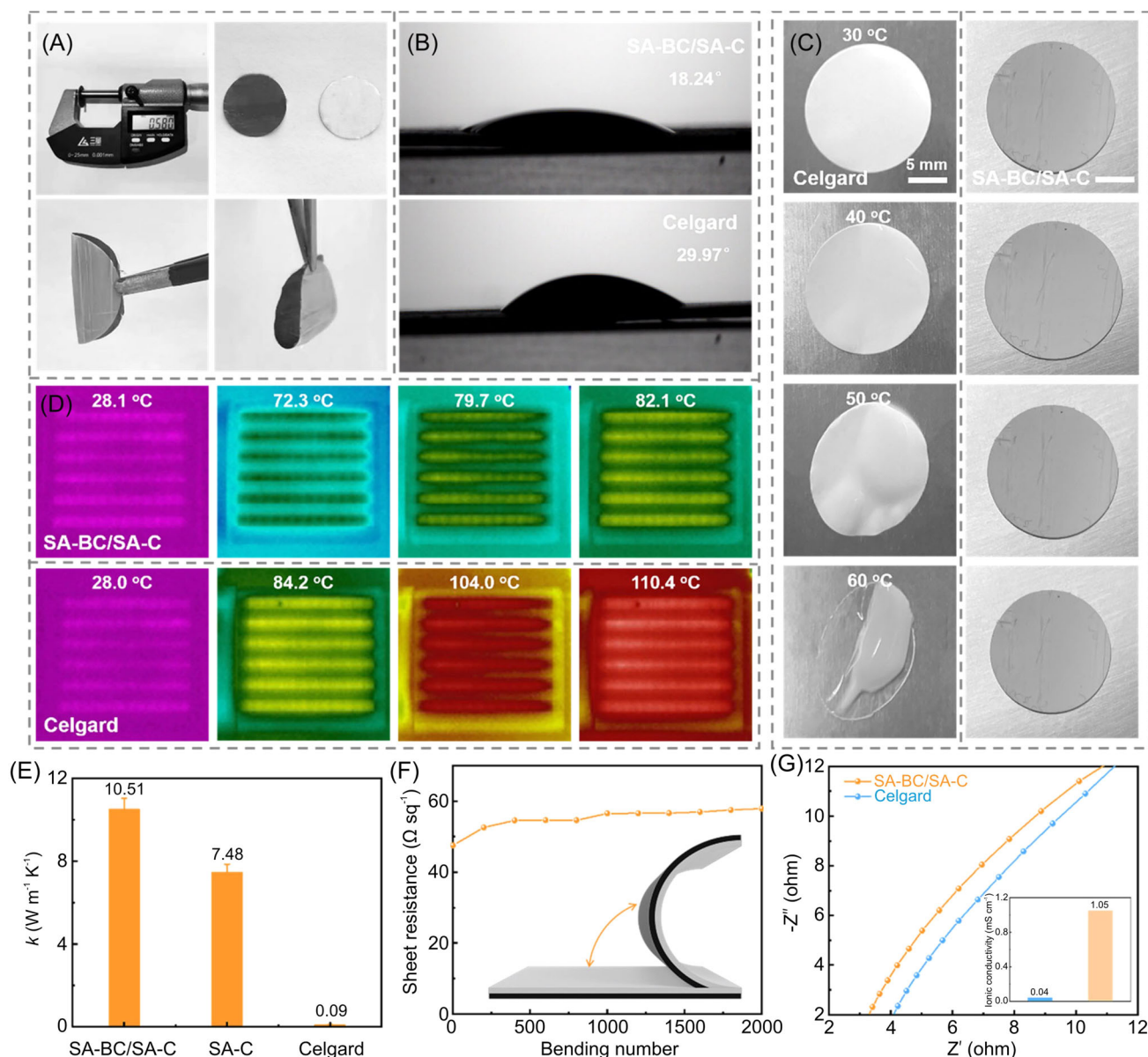


FIGURE 3 Physical characterization of the SA-BC/SA-C separator. (A) Thickness and flexibility measurement of the SA-BC/SA-C separator. (B) Wettability, (C) temperature tolerance, and (D) heat-dissipation performance of the Celgard and SA-BC/SA-C separators. (E) In-plane thermal conductivity of SA-BC/SA-C, SA-C, and Celgard. (F) Variation in the sheet resistance of the SA-BC/SA-C separator during repeated bending. (G) Ionic conductivity of the SA-BC/SA-C and Celgard separators.

to evacuate the accumulated heat in an efficient manner, which would prevent thermal runaway caused by high local temperatures. In-plane thermal conductivity measurements were conducted to elucidate the mechanism of the separator's thermal management performance. As shown in Figure 3E, the SA-BC/SA-C separator showed a thermal conductivity of 10.51 W m⁻¹ K⁻¹, which was much higher than that of the Celgard separator (0.09 W m⁻¹ K⁻¹).

The SA-BC/SA-C separator also had good mechanical properties and could physically inhibit the growth of Li dendrites, thereby preventing short-circuiting and

showing potential utility for the construction of flexible wearable devices. Figures 3F and S8 show the schematic illustration of repeated bending of the SA-BC/SA-C separator and the change of the square resistance on one side of the SA-C film. After 2000 repeated bending operations, the separator maintained a low square resistance (57.87 Ω sq⁻¹), corresponding to an increase of 0.011% per bend. SEM were also used to observe changes in the surface morphology on one side of the SA-BC film after repeated bending. As shown in Figure S9, the SA-BC/SA-C separator maintained an unaltered morphology, but the bare SA-BC separator showed

fractured nanobundles. These results indicate that the SA-C film could effectively release the stress generated during repeated bending, endowing the composite with useful mechanical properties. The Nyquist curves of the SA-BC/SA-C symmetric batteries showed the smallest Z-axis intercept, indicating that they had the lowest bulk resistance of all of the batteries that were compared. They also had the highest ionic conductivity (1.05 mS cm^{-1}) of all of the batteries that were compared, indicating that the ionic conductivity of the SA-BC/SA-C separator meets the requirements of commercial LSBs (Figure 3G).

The synergy between the molecular brush effect and the vertical super-aligned structure of the SA-BC/SA-C separator means that its straight ion-transport channels enable uniform ion flow. This promotes the smooth deposition of Li by considerably lowering local ion concentrations, and thus inhibits the growth of Li dendrites (Figure 4A). In contrast, the zigzag ion-transport channels in the commercial Celgard separator led to uneven distributions of ion concentrations, leading to considerable Li dendrite growth (Figure 4B). The electrochemical performance of the symmetrical batteries was also tested to verify the ability of the SA-BC/SA-C separator to inhibit the growth of Li dendrites. As shown in Figure 4C,D, the symmetrical battery with an SA-BC/SA-C separator presented a stable overpotential (23 mV) over 500 cycles at a low current density (1 mA cm^{-2}) with a stripping/plating capacity of 1 mAh cm^{-2} . In contrast, the overpotential of the Celgard separator fluctuated considerably and the battery eventually short-circuited. A high current density was also used to demonstrate the superiority of the super-aligned structure of our separator. When the current density was increased to 5 mA cm^{-2} , the SA-BC/SA-C separator showed good cycle stability with a low overpotential (31 mV) over 1000 cycles, outperforming the Celgard separator (Figure S10). Even at a higher current density (10 mA cm^{-2}), the SA-BC/SA-C separator maintained a stable overpotential (40 mV) over 1000 cycles. In contrast, the Celgard separator showed a rapidly increasing overpotential (Figure 4E,F).

To intuitively demonstrate the superiority of the SA-BC/SA-C separator, the cycle performance was further compared with that of the separator in recent studies of separator modification (Figure 4H and Table S1). Under a high current density (10 mA cm^{-2}), the SA-BC/SA-C separator had much higher cycle stability than most previously reported separators. The rate performance of the symmetric batteries with an SA-BC/SA-C separator was further assessed at current densities of 1, 3, 5, and 10 mA cm^{-2} at a fixed capacity of 1 mAh cm^{-2} . As shown in Figure 4G, the SA-BC/SA-C separator showed a

reversible overpotential that was consistent with the overpotential value of the long-term cycle performance. In contrast, the Celgard separator showed poorly reversible rate performance with an unstable overpotential. Moreover, even under a high stripping/plating capacity of 3 and 5 mAh cm^{-2} , the symmetric batteries with an SA-BC/SA-C separator still maintained excellent cyclic stability, demonstrating the significant advantage of the separator in inhibiting dendrite growth (Figure S11).

Coulombic efficiency (CE) is an important parameter for assessing the stability and practicality of separators. As shown in Figure S12, the CE curves of the SA-BC/SA-C and the Celgard separators were obtained by measuring symmetrical batteries containing each of these separators at a current density of 5 mA cm^{-2} and with a Li-stripping/plating capacity of 10 mAh cm^{-2} . The SA-BC/SA-C separator showed a steady CE curve and maintained a high CE value (98.5%) over 50 cycles, while the Celgard separator showed an unstable CE curve with large fluctuations. The excellent electrochemical performance of the SA-BC/SA-C separator further demonstrated the rationality and practicality of its delicate structural design for uniformizing Li-ion flow and inhibiting Li dendrite growth to prevent short-circuiting and subsequent thermal runaway.

In addition to the uniform thermal field of the SA-BC/SA-C separator rapidly evacuating the heat inside an LSB, the effective control of polysulfides also alleviated heat accumulation. Thus, a static adsorption experiment was conducted to directly observe the ability of the SA-BC/SA-C separator to adsorb and anchor polysulfides. Over 24 h, an original brown solution of lithium hexasulfide (Li_2S_6 , 8 mmol L^{-1}) gradually became colorless when the SA-BC/SA-C separator was used, but the solution had the same color as the original blank sample when the Celgard separator was used (Figure S13). These results suggest that the SA-BC/SA-C separator was better able to adsorb and anchor the polysulfides than the Celgard separator. Ultraviolet-visible light-absorption analysis was also performed to assess the ability of the SA-BC/SA-C separator to adsorb polysulfides. As shown in Figure S14, the SA-BC/SA-C separator showed a much weaker absorption peak for polysulfides than the Celgard separator, implying that the former separator had more effectively adsorbed the polysulfides than the latter separator. To clarify the mechanism of polysulfide adsorption, XPS measurements were performed after the separators had absorbed a Li_2S_6 solution for 24 h (Figure S15). In the high-resolution S 2p spectrum of the SA-BC/SA-C separator, there was a distinct peak at 167.00 eV, which represents a $\text{S}\cdots\text{B}=\text{N}$ interaction, implying that there is a strong interaction between BN and polysulfides in this separator. This interaction is responsible for the strong polysulfide

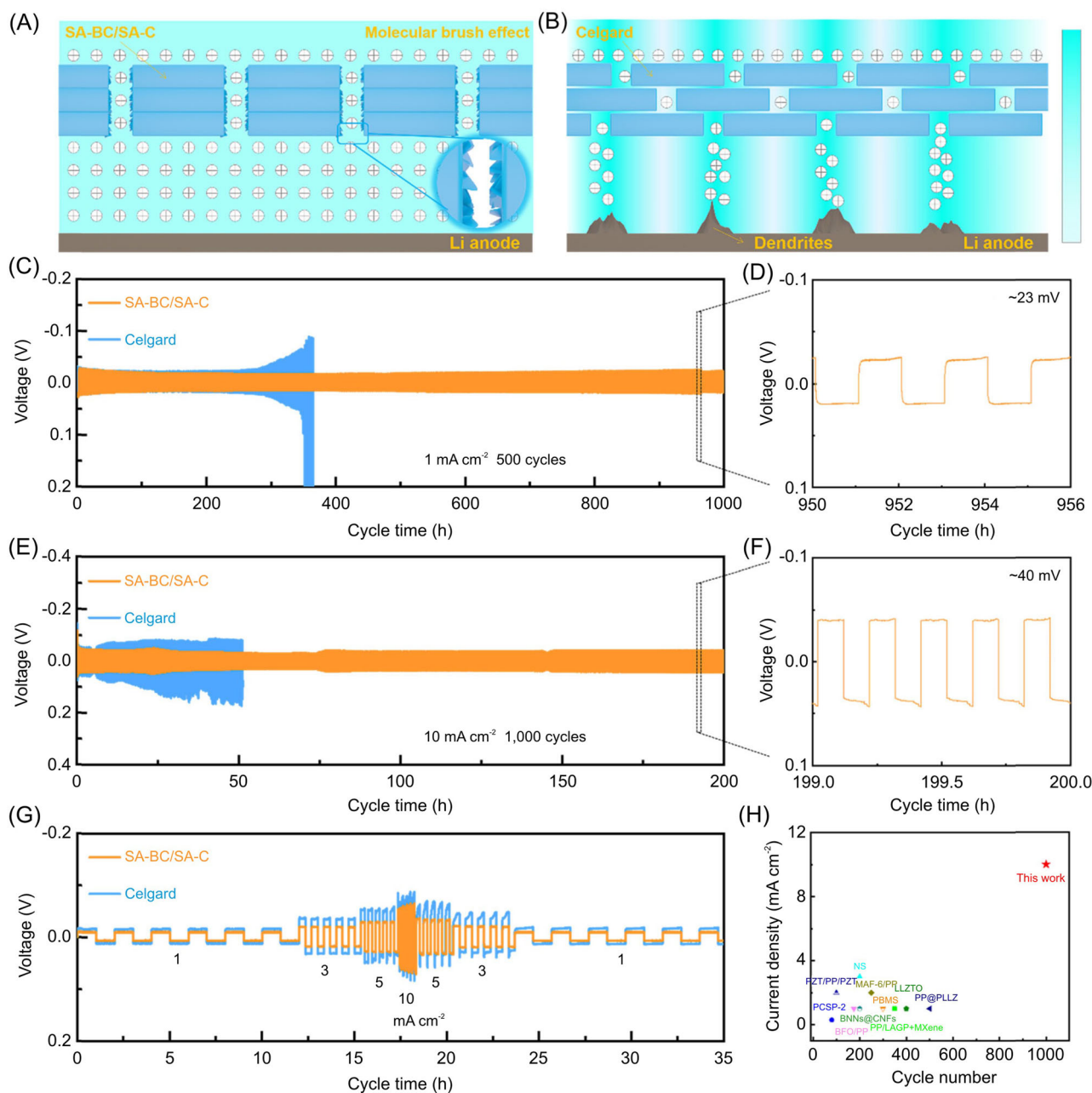


FIGURE 4 SA-BC/SA-C separator inhibition of Li dendrites. (A) Schematic illustration of ion concentration and Li-deposition behavior in lithium–sulfur batteries (LSBs) equipped with SA-BC/SA-C and (B) Celgard separators. Cycle performance of symmetric LSBs with each separator at current densities of (C) 1 mA cm^{-2} and (E) 10 mA cm^{-2} with a constant capacity of 1 mAh cm^{-2} . (D, F) The enlarged images on the right show details of the overpotential as a function of cycle time. (G) Rate performance of symmetric batteries with each separator. (H) Cycle lifespan of symmetric batteries equipped with the SA-BC/SA-C separator compared with those equipped with other separators at various current densities and with a constant capacity of 1 mAh cm^{-2} .^{48–57}

adsorption and anchoring effect of the SA-BC/SA-C separator.⁵⁸

The ability of different separators to inhibit polysulfide shuttling was further investigated by monitoring the shuttle current of LSBs (Figure S16). Generally, the tested LSBs were subjected to galvanostatic discharge to 2.38 V and then remained in a potentiostatic state that generated a shuttle current. The SA-BC/SA-C separator

showed the smallest shuttle current, indicating strong polysulfide adsorption and anchoring that would inhibit polysulfide shuttling. The ability to strongly anchor polysulfides is a prerequisite for accelerating the redox kinetics of polysulfides, which can be investigated using cyclic voltammetry (CV) tests. CV tests were thus performed for three cycles to explore the reversibility of an LSB equipped with the SA-BC/SA-C separator. The

CV curves almost exactly coincide, suggesting that the LSB had good reversibility owing to the ability of the SA-BC/SA-C separator to anchor polysulfides (Figure 5A). The LSB with the SA-C/SA-BC separators showed smaller voltage gaps between redox peaks than the LSBs with SA-C or Celgard separators, implying that the SA-BC/SA-C separator has a strong polysulfide anchoring effect that led to fast redox kinetics (Figure S17), which is consistent with the charge–discharge curve results at a current density of 0.5 C. As shown in Figure 5B, the battery with the SA-BC/SA-C separator delivered the smallest voltage gap (116 mV) between two tangents of the voltage platform, while the batteries with SA-BC and Celgard separators delivered voltage gaps of 149 and 152 mV, respectively.

Unlike traditional commercial separators with zigzag ion-transport channels, the two-layer super-aligned separator (i.e., the SA-BC/SA-C separator) had straight ion-

transport channels that enhanced the redox kinetics of LSBs. As the internal resistance of charge transfer and electrolyte diffusion are important indexes that are used to evaluate polysulfide adsorption, the electrochemical impedance spectroscopy curves were compared to investigate how the separators promoted charge transfer (Figure S18). Compared with the SA-BC and Celgard separators, the SA-BC/SA-C separator had lower transfer resistance and increased Li^+ diffusion kinetics. Typically, BN causes the accumulation of polysulfides and cannot fundamentally solve the polysulfide shuttling effect. However, the introduction of highly conductive CNTs in the SA-C/SA-BC separator helped to regulate polysulfide charge transfer and thus suppressed polysulfide shuttling, thereby enhancing the redox kinetics of an LSB battery.

Owing to the positive effects of the SA-BC/SA-C separator in increasing heat dissipation, decreasing polysulfide shuttling, and inhibiting the growth of Li

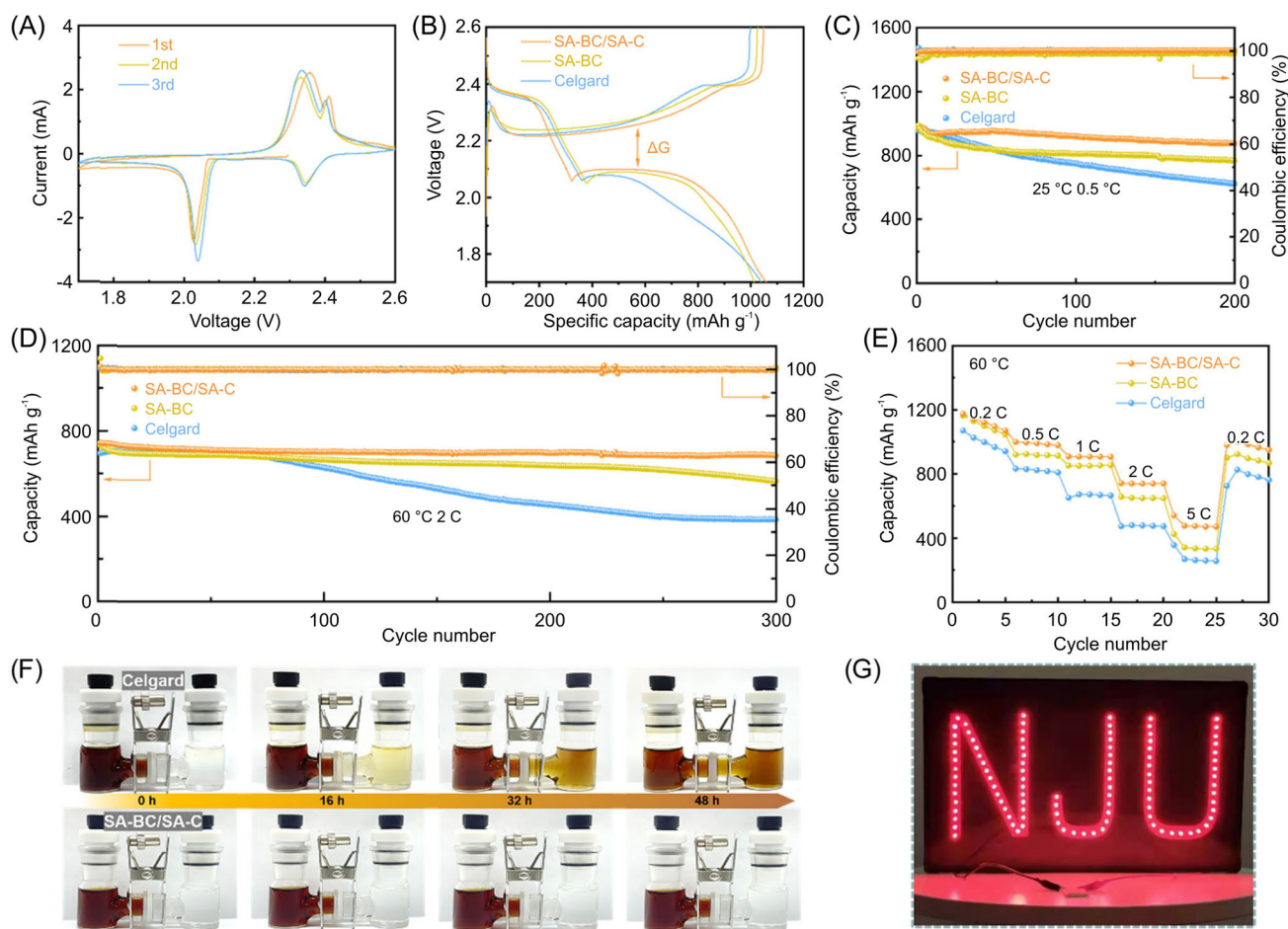


FIGURE 5 Electrochemical performances of LSBs. (A) The first three cyclic voltammetry curves for LSBs equipped with the SA-BC/SA-C separator. (B) Galvanostatic charge–discharge profiles of various separators at 0.5 C. (C) Cycle performance of LSBs equipped with various separators at 0.5 C and 25°C. (D) Cycle performance of LSBs equipped with various separators at 2 C and 60°C. (E) Rate performance of LSBs with equipped various separators at different current densities at 60°C. (F) Visualization tests of polysulfides blocking the Celgard and the SA-BC/SA-C separators. (G) Li-S pouch cell with the SA-BC/SA-C separator continuously powering a light-emitting diode indicator.

dendrites, an LSB battery containing this separator showed good cycle performance at various temperatures. As shown in Figure 5C, the LSB equipped with the SA-BC/SA-C separator had a high discharge capacity (875.2 mAh g⁻¹) with a high CE (~100%) over 200 cycles at 0.5 C and 25°C. In contrast, the LSBs equipped with SA-BC or Celgard separators had lower capacities (767.6 and 622.1 mAh g⁻¹, respectively) that rapidly decayed over 200 cycles. When the current density was increased to 2 C, the discharge capacity of the SA-BC/SA-C separator slowly decreased to 622.6 mAh g⁻¹ over 300 cycles, while those of the SA-BC and Celgard separators rapidly decreased to 521.3 mAh g⁻¹ and 456.5 mAh g⁻¹, respectively (Figure S19A). The cycle performance of LSBs at high temperatures can reflect the heat-management capability of their separators. At 60°C, the LSB equipped with the SA-BC/SA-C separator showed stable discharge capacity (1003.4 mAh g⁻¹ at 0.5 C) over 200 cycles; this was far better than the cycle performance of the LSBs with SA-BC and Celgard separators, which showed capacities of 879.7 and 451.3 mAh g⁻¹, respectively (Figure S19B). When the current density was increased to 2 C, the LSB equipped with the SA-BC/SA-C separator showed a discharge capacity of 685.2 mAh g⁻¹ over 300 cycles (a capacity decay of 0.026% per cycle), outperforming the LSBs equipped with SA-BC or Celgard separators, which had discharge capacities of 565.5 mAh g⁻¹ (a capacity decay of 0.076% per cycle) and 387.5 mAh g⁻¹ (a capacity decay of 0.147% per cycle), respectively (Figure 5D). The reason for the rapid capacity decay at high temperatures was revealed by postmortem analysis of the cycled LSBs (Figure S20). The cycled Celgard separator showed a folded surface with a dark-yellow precipitate, indicating that its low temperature durability and inadequate polysulfide conversion accounted for the rapid capacity decay of the battery in which it was fitted. In contrast, the conductive CNTs of the SA-BC/SA-C separator facilitated the rapid charge transfer of polysulfides in the redox process, which promoted the conversion of high-valence polysulfides into low-valence polysulfides, thereby preventing polysulfide accumulation. Moreover, the BN nanosheets of the SA-BC/SA-C separator had high thermal conductivity and good temperature durability. Thus, the SA-BC/SA-C separator showed a flat surface with a light-yellow precipitate, and the LSB in which it was fitted showed slow capacity decay. These results demonstrate that the SA-BC/SA-C separator could inhibit polysulfide shuttling and Li dendrite growth, and also dissipated the heat generated inside the LSB.

The rate performance of the separators was measured at 60°C. As shown in Figure 5E, the LSB equipped with the SA-BC/SA-C separator had high discharge capacities:

1173.4, 998.9, 907.9, 741.1, and 541.5 mAh g⁻¹ at cycling rates of 0.2, 0.5, 1, 2, and 5 C, respectively. Upon switching back to 0.2C, this LSB retained 84% of its initial capacity, which was far better than that retained by the LSB equipped with the SA-BC or Celgard separators. This confirmed the good reversibility and heat regulation performance of the LSB with the SA-BC/SA-C separator. Figure S21 shows the same rate performance of the separator at a lower temperature (25°C).

The electrochemical performance of LSBs under high S loadings was used to evaluate whether the SA-BC/SA-C separator could be used in the fabrication of energy storage devices with high energy density. As shown in Figure S22, the battery with a S loading of 3 mg cm⁻² had stable discharge capacity (588.6 mAh g⁻¹) over 100 cycles at a current density of 0.3 C. Meanwhile, the battery with an areal capacity of 3 mAh cm⁻² delivered an excellent discharge capacity of 593.5 mAh g⁻¹ over 100 cycles at 0.5 C (Figure S23). It is worth noting that the excellent electrochemical performance of LSBs is closely related to their control of Li dendrite growth. To further investigate the effect of the SA-BC/SA-C separator in blocking polysulfide diffusion, an H-type electrolytic cell was prepared with the separator placed between two different electrolytes. When the Celgard separator was used, the electrolyte color on both sides of the electrolytic cell turned the same brown color, suggesting that the commercial Celgard separator failed to inhibit polysulfide diffusion (Figure 5F). In contrast, when the SA-BC/SA-C separator was used, the electrolyte color did not change over 48 h, indicating that this separator was able to block polysulfide diffusion. To assess the practicability of the separator, a pouch battery was assembled to investigate its ability to discharge continuously (Figure S24). As shown in Figure 5G, the LED displayed a steady and bright light, suggesting the potential commercial value of the designed separator. Based on these results, this highly thermally conductive separator can be used to fabricate safe LSBs with enhanced electrochemical performance.

To mitigate the safety problems in LSBs that can lead to thermal runaway, our three-dimensional self-supporting SA-BC/SA-C separator was constructed via phase selection and structure optimization (Figure 6). By combining the high thermal conductivity of BN and CNTs in a super-aligned staggered structure, a uniform thermal field was obtained, as shown in Figure 6A. This configuration was different from that of Celgard, which has an uneven thermal field (Figure S25). To demonstrate that the constructed heat conduction pathway could alleviate the safety problems related to electrolyte decomposition caused by heat accumulation, we conducted finite element method (FEM) analysis of the electrolyte heat distribution near the separators. As

shown in Figure 6B, the SA-BC/SA-C separator effectively reduced heat buildup in the electrolyte, thereby improving the overall safety of an LSB. In contrast, the Celgard separator showed relatively high heat and an uneven electrolyte heat distribution (Figures 6C and S26).

To further demonstrate the application potential of the SA-BC/SA-C separator in LSBs, the electrolyte density distribution near the separator was simulated by FEM analysis. In contrast to the Celgard separator, which had uneven pores and zigzag ion channels resulting from mechanical stretching (Figure 6F), the SA-BC/SA-C separator achieved a uniform ion concentration in the electrolyte owing to its high flux and straight ion-transport

channels, demonstrating that the composite fibers in the SA-BC/SA-C separator acted as a molecular brush to regulate local ion concentrations and ion flux (Figures 6E and S27). We also simulated the electron conduction to demonstrate the role of the SA-BC/SA-C separator in the catalytic conversion of polysulfides. The high electronic conductivity of CNTs in the SA-BC/SA-C significantly reduced the local current density, thereby promoting the catalytic conversion of polysulfides and thus preventing the loss of active substances caused by the accumulation of polysulfides (Figure 6D).

Atomic force microscopy and Kelvin probe force microscopy were used to investigate the surface morphology and surface potential of the SA-BC/SA-C separator. The

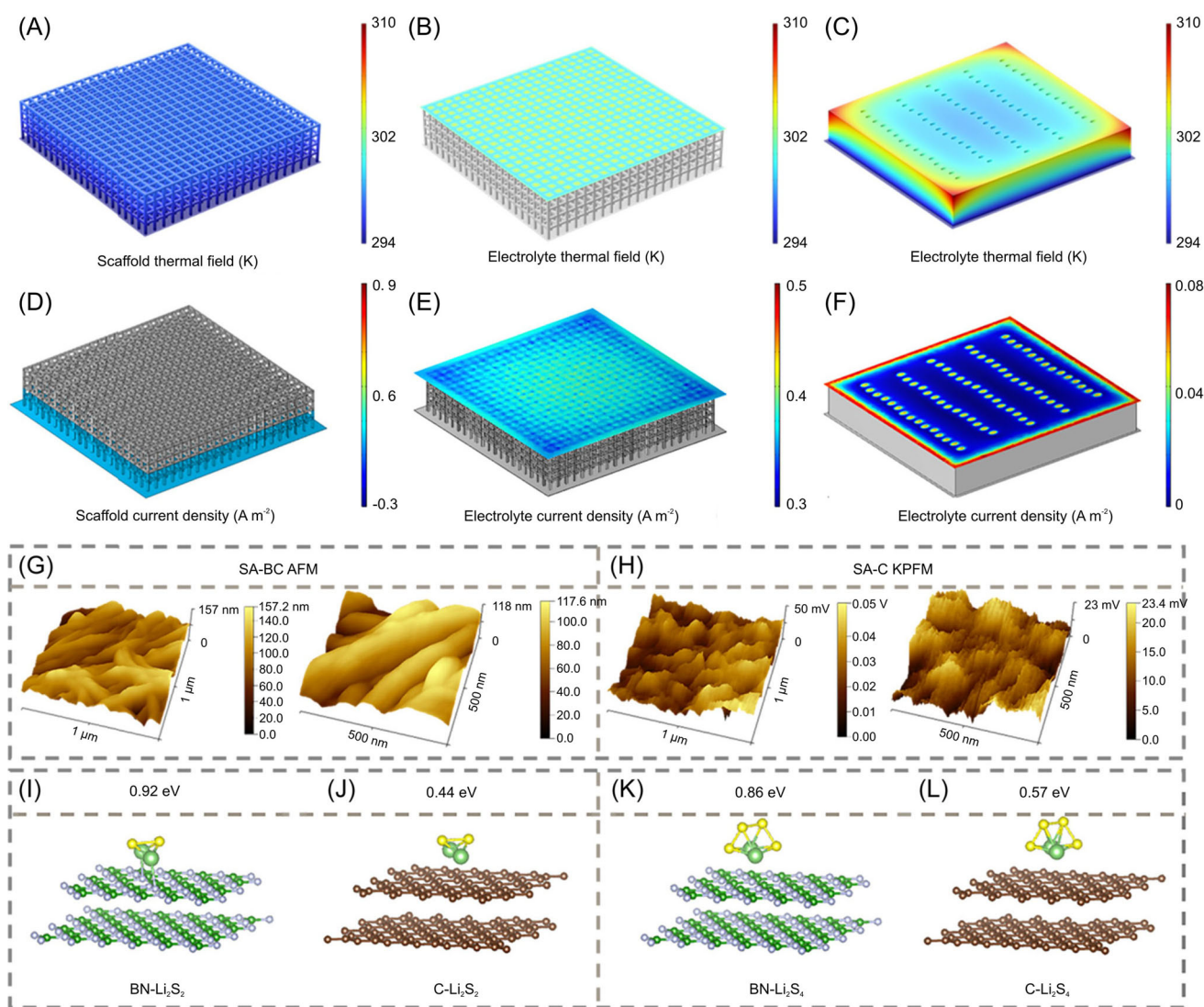


FIGURE 6 Simulation of the rational design of the separator structure. (A) Simulation of the thermal field distribution in the SA-BC/SA-C separator. Heat distribution of electrolyte near (B) the SA-BC/SA-C and (C) Celgard separators. (D) Current density distribution of the SA-BC/SA-C separator. Local distribution of ion concentration in the electrolyte near (E) the SA-BC/SA-C and (F) Celgard separators. (G, H) Atomic force microscopy (AFM) and Kelvin probe force microscopy (KPFM) images of the SA-BC/SA-C separator. (I–L) Polysulfide adsorption configurations and adsorption energies of boron nitride and carbon.

SA-BC side of the separator showed a fibrous morphology owing to the BN nanofibers, with a low roughness (118 nm; Figure 6G,H). The SA-C side had a uniform surface potential of 23 mV due to the super-aligned staggered CNTs. In addition, density functional theory calculations were carried out to simulate the polysulfide adsorption capacity of the BN and C. As shown in Figure 6I-L, BN showed dilithium disulfide and dilithium tetrasulfide adsorption energies of 0.92 and 0.86 eV, respectively, which were higher than those for C (0.44 and 0.57 eV, respectively). These high adsorption energies indicate that strong polysulfide anchoring occurred in the SA-BC/SA-C separator. These results clearly demonstrate that the SA-BC/SA-C separator can dissipate accumulated heat, suppress polysulfide shuttling, and hinder Li dendrite growth.

3 | CONCLUSION

We constructed a highly thermally conductive separator by cross-weaving super-aligned CNTs on super-aligned BN@CNTs to create a composite film that efficiently evacuated accumulated heat from an LSB. The double-layer super-aligned structure with a homogeneous thermal field enabled the rapid dispersion of the heat generated by an LSB's internal resistance during the charging and discharging processes, and thus prevented a continuous increase in temperature. The straight ion-transport channels and smooth electron conduction of the SA-BC/SA-C separator meant that it effectively captured high-valence polysulfides and accelerated their catalytic conversion into low-valence polysulfides. The synergy between the molecular brush effect and the vertical super-aligned structure homogenized the ion flow, considerably decreasing local ion concentrations and thus inhibiting Li dendrite growth, and thus promoted the smooth deposition of Li metal. These features allowed symmetric LSBs containing the SA-BC/SA-C separator to maintain a stable overpotential (40 mV) over 1000 cycles at a high current density (10 mA cm⁻²). LSBs equipped with the SA-BC/SA-C separator also showed a good discharge capacity (685.2 mAh g⁻¹ over 300 cycles, with a capacity decay of 0.026% per cycle) at 2 C and 60°C. Our strategy based on the design of a super-aligned structure led to the fabrication of a separator with high thermal conductivity. This constitutes a new approach for the fabrication of safer LSBs with enhanced electrochemical performance.

ACKNOWLEDGMENTS

This work was funded by the National Key R&D Program of China (Grant No. 2022YFE0206500).

CONFLICTS OF INTEREST STATEMENT

The authors declare no conflicts of interest.

ORCID

Jun Pu  <http://orcid.org/0000-0001-9393-3798>

Qiang Zhang  <http://orcid.org/0000-0002-3929-1541>

Yagang Yao  <http://orcid.org/0000-0002-4381-2952>

REFERENCES

- Pang Q, Shyamsunder A, Narayanan B, Kwok CY, Curtiss LA, Nazar LF. Tuning the electrolyte network structure to invoke quasi-solid state sulfur conversion and suppress lithium dendrite formation in Li-S batteries. *Nat Energy*. 2018;3(9):783-791.
- Liu Y, Elias Y, Meng J, et al. Electrolyte solutions design for lithium-sulfur batteries. *Joule*. 2021;5(9):2323-2364.
- Liu YT, Liu S, Li GR, Gao XP. Strategy of enhancing the volumetric energy density for lithium-sulfur batteries. *Adv Mater*. 2021;33(8):2003955.
- Luo S, Wu F, Yushin G. Strategies for fabrication, confinement and performance boost of Li₂S in lithium sulfur, silicon-sulfur & related batteries. *Mater Today*. 2021;49(1):253-270.
- Zhou L, Danilov DL, Eichel RA, Notten PHL. Host materials anchoring polysulfides in Li-S batteries reviewed. *Adv Energy Mater*. 2020;11(15):2001304.
- Yang H, Guo C, Chen J, et al. An intrinsic flame-retardant organic electrolyte for safe lithium sulfur batteries. *Angew Chem Int Ed*. 2019;58(3):791-795.
- Chen X, Xiao Z, Ning X, et al. Sulfur-impregnated, sandwich-type, hybrid carbon nanosheets with hierarchical porous structure for high-performance lithium-sulfur batteries. *Adv Energy Mater*. 2014;4(13):1301988.
- Wang J, Lin F, Jia H, Yang J, Monroe CW, NuLi Y. Towards a safe lithium-sulfur battery with a flame-inhibiting electrolyte and a sulfur-based composite cathode. *Angew Chem*. 2014;126(38):10263-10268.
- Guo Q, Zheng Z. Rational design of binders for stable Li-S and Na-S batteries. *Adv Funct Mater*. 2019;30(6):1907931.
- Wu H, Zhuo D, Kong D, Cui Y. Improving battery safety by early detection of internal shorting with a bifunctional separator. *Nat Commun*. 2014;5(1):5193.
- Kitazawa Y, Iwata K, Kido R, et al. Polymer electrolytes containing solvate ionic liquids: a new approach to achieve high ionic conductivity, thermal stability, and a wide potential window. *Chem Mater*. 2017;30:252-261.
- Liu K, Liu Y, Lin D, Pei A, Cui Y. Materials for lithium-ion battery safety. *Sci Adv*. 2018;4(6):eaas9820.
- Feng X, Ouyang M, Liu X, Lu L, Xia Y, He X. Thermal runaway mechanism of lithium ion battery for electric vehicles: a review. *Energy Storage Mater*. 2018;10:246-267.
- Feng X, Ren D, He X, Ouyang M. Mitigating thermal runaway of lithium-ion batteries. *Joule*. 2020;4(4):743-770.
- Finegan DP, Scheel M, Robinson JB, et al. In-operando high-speed tomography of lithium-ion batteries during thermal runaway. *Nat Commun*. 2015;6:6924.
- Finegan DP, Darcy E, Keyser M, et al. Characterising thermal runaway within lithium-ion cells by inducing and monitoring internal short circuits. *Energy Environ Sci*. 2017;10(6):1377-1388.
- Zeng Y, Chalish D, Lubner SD, Kaur S, Prasher RS. A review of thermal physics and management inside lithium-ion batteries for high energy density and fast charging. *Energy Storage Mater*. 2021;41(1):264-288.

18. Hao M, Li J, Park S, Moura S, Dames C. Efficient thermal management of Li-ion batteries with a passive interfacial thermal regulator based on a shape memory alloy. *Nat Energy*. 2018;3(10):899-906.
19. Ji W, Wang F, Liu D, et al. Building thermally stable Li-ion batteries using a temperature-responsive cathode. *J Mater Chem A*. 2016;4(29):11239-11246.
20. Shi Y, Zhang Q, Zhang Y, Jia L, Xu X. Promising and reversible electrolyte with thermal switching behavior for safer electrochemical storage devices. *ACS Appl Mater Interfaces*. 2018;10(8):7171-7179.
21. Wen L, Liang J, Chen J, Chu ZY, Cheng HM, Li F. Smart materials and design toward safe and durable lithium ion batteries. *Small Methods*. 2019;3(11):1900323.
22. Luo W, Zhou L, Fu K, et al. A thermally conductive separator for stable Li metal anodes. *Nano Lett*. 2015;15(9):6149-6154.
23. Liu Y, Qiao Y, Zhang Y, et al. 3D printed separator for the thermal management of high-performance Li metal anodes. *Energy Storage Mater*. 2018;12(1):197-203.
24. Kim PJH, Pol VG. Surface functionalization of a conventional polypropylene separator with an aluminum nitride layer toward ultrastable and high-rate lithium metal anodes. *ACS Appl Mater Interfaces*. 2019;11(4):3917-3924.
25. Zhao B, Jiang L, Zeng X, et al. A highly thermally conductive electrode for lithium ion batteries. *J Mater Chem A*. 2016;4(38):14595-14604.
26. Liu Z, Hu Q, Guo S, Yu L, Hu X. Thermoregulating separators based on phase-change materials for safe lithium-ion batteries. *Adv Mater*. 2021;33(15):2008088.
27. Zhang H, Judez X, Santiago A, et al. Fluorine-free noble salt anion for high-performance all-solid-state lithium-sulfur batteries. *Adv Energy Mater*. 2019;9(25):1900763.
28. Xu J, An S, Song X, et al. Towards high performance Li-S batteries via sulfonate-rich COF-modified separator. *Adv Mater*. 2021;33(49):2105178.
29. Shi Z, Sun Z, Cai J, et al. Manipulating electrocatalytic Li₂S redox via selective dual-defect engineering for Li-S batteries. *Adv Mater*. 2021;33(43):2103050.
30. Xue P, Zhu K, Gong W, et al. "One stone two birds" design for dual-functional TiO₂-TiN heterostructures enabled dendrite-free and kinetics-enhanced lithium-sulfur batteries. *Adv Energy Mater*. 2022;12(18):2200308.
31. Xue P, Guo C, Li L, et al. A MOF-derivative decorated hierarchical porous host enabling ultrahigh rates and superior Long-Term cycling of Dendrite-Free Zn metal anodes. *Adv Mater*. 2022;34(14):2110047.
32. Cheng Z, Pan H, Chen J, Meng X, Wang R. Separator modified by cobalt-embedded carbon nanosheets enabling chemisorption and catalytic effects of polysulfides for high-energy-density lithium-sulfur batteries. *Adv Energy Mater*. 2019;9(32):1901609.
33. Qian J, Chen Q, Hong M, et al. Toward stretchable batteries: 3D-printed deformable electrodes and separator enabled by nanocellulose. *Mater Today*. 2022;54:18-26.
34. Chen Y, Wang T, Tian H, Su D, Zhang Q, Wang G. Advances in lithium-sulfur batteries: from academic research to commercial viability. *Adv Mater*. 2021;33(29):2003666.
35. Li S, Zhang W, Zheng J, Lv M, Song H, Du L. Inhibition of polysulfide shuttles in Li-S batteries: modified separators and solid-state electrolytes. *Adv Energy Mater*. 2021;11(2):2000779.
36. Fang D, Wang Y, Liu X, et al. Spider-web-inspired nanocomposite modified separator: structural and chemical cooperativity inhibiting the shuttle effect in Li-S batteries. *ACS Nano*. 2019;13(2):1563-1573.
37. Wu Z, Chen S, Wang L, et al. Implanting nickel and cobalt phosphide into well-defined carbon nanocages: a synergistic adsorption-electrocatalysis separator mediator for durable high-power Li-S batteries. *Energy Storage Mater*. 2021;38:381-388.
38. Zhu K, Xue P, Cheng G, et al. Thermo-managing and flame-retardant scaffolds suppressing dendritic growth and polysulfide shuttling toward high-safety lithium-sulfur batteries. *Energy Storage Mater*. 2021;43:130-142.
39. Cai Q, Scullion D, Gan W, et al. High thermal conductivity of high-quality monolayer boron nitride and its thermal expansion. *Sci Adv*. 2019;5(6):eaav0129.
40. Zheng L, Liu Z, Liu D, et al. Deep subwavelength control of valley polarized cathodoluminescence in h-BN/WSe₂/h-BN heterostructure. *Nat Commun*. 2021;12:291.
41. Kim G, Ma KY, Park M, et al. Blue emission at atomically sharp 1D heterojunctions between graphene and h-BN. *Nat Commun*. 2020;11:5359.
42. Li T, Wang L, Zhang K, et al. Freestanding boron nitride nanosheet films for ultrafast oil/water separation. *Small*. 2016;12(36):4960-4965.
43. Zhu Z, Wei N, Cheng W, et al. Rate-selected growth of ultrapure semiconducting carbon nanotube arrays. *Nat Commun*. 2019;10:4467.
44. Kim SY, Park J, Choi HC, Ahn JP, Hou JQ, Kang HS. X-ray photoelectron spectroscopy and first principles calculation of BCN nanotubes. *J Am Chem Soc*. 2007;129(6):1705-1716.
45. Gao Y, Ren W, Ma T, et al. Repeated and controlled growth of monolayer, bilayer and few-layer hexagonal boron nitride on pt foils. *ACS Nano*. 2013;7(6):5199-5206.
46. Ye M, Xiao Y, Cheng Z, Cui L, Jiang L, Qu L. A smart, anti-piercing and eliminating-dendrite lithium metal battery. *Nano Energy*. 2018;49(1):403-410.
47. Peng HJ, Wang DW, Huang JQ, et al. Janus separator of polypropylene-supported cellular graphene framework for sulfur cathodes with high utilization in lithium-sulfur batteries. *Adv Sci*. 2016;3(1):1500268.
48. Xue L, Chen W, Hu Y, et al. Ferroelectric polarization accelerates lithium-ion diffusion for dendrite-free and highly-practical lithium-metal batteries. *Nano Energy*. 2021;79(1):105481.
49. Huo H, Li X, Chen Y, et al. Bifunctional composite separator with a solid-state-battery strategy for dendrite-free lithium metal batteries. *Energy Storage Mater*. 2020;29(1):361-366.
50. Wu X, Liu N, Guo Z, et al. Constructing multi-functional Janus separator toward highly stable lithium batteries. *Energy Storage Mater*. 2020;28(1):153-159.
51. Wu WL, Xu YT, Ke X, et al. Superorganophilic MAF-6/PP composite separator boosts lithium metal anode performance. *Energy Storage Mater*. 2021;37(1):387-395.
52. Han X, Chen J, Chen M, et al. Induction of planar Li growth with designed interphases for dendrite-free Li metal anodes. *Energy Storage Mater*. 2021;39(1):250-258.

53. Hu Z, Liu F, Gao J, et al. Dendrite-free lithium plating induced by in situ transferring protection layer from separator. *Adv Funct Mater.* 2019;30(5):1907020.
54. Li Y, Gao T, Ni D, et al. Two birds with one stone: interfacial engineering of multifunctional Janus separator for lithium-sulfur batteries. *Adv Mater.* 2022;34(5):2107638.
55. Liang J, Chen Q, Liao X, et al. A nano-shield design for separators to resist dendrite formation in lithium-metal batteries. *Angew Chem Int Ed.* 2020;59(16):6561-6566.
56. Gao GK, Wang YR, Wang SB, et al. Stepped channels integrated lithium-sulfur separator via photoinduced multi-dimensional fabrication of metal-organic framework. *Angew Chem Int Ed.* 2021;60(18):10147-10154.
57. Zhao CZ, Chen PY, Zhang R, et al. An ion redistributor for dendrite-free lithium metal anodes. *Sci Adv.* 2018;4(11):eaat3446.
58. Xia D, Li H, Huang P, et al. Boron-nitride/carbon-nanotube hybrid aerogels as multifunctional desulfurisation agents. *J Mater Chem A.* 2019;7(41):24027-24037.

SUPPORTING INFORMATION

Additional supporting information can be found online in the Supporting Information section at the end of this article.

How to cite this article: Zhu K, Li L, Xue P, et al. “Three-in-one” strategy: Heat regulation and conversion enhancement of a multifunctional separator for safer lithium-sulfur batteries. *Carbon Energy.* 2023;5:e352. doi:10.1002/cey2.352